Extended magnetohydrodynamics simulations of thin-foil Z-pinch implosions with comparison to experiments

J. M. Woolstrum (iD), D. A. Yager-Elorriaga, P. C. Campbell, N. M. Jordan (iD), C. E. Seyler (iD), and R. D. McBride (iD)

View Online   Export Citation   CrossMark

Extended magnetohydrodynamics simulations of thin-foil Z-pinch implosions with comparison to experiments

J. M. Woolstrum,[1,a] D. A. Yager-Elorriaga,[2] P. C. Campbell,[1] N. M. Jordan,[1] C. E. Seyler,[3] and R. D. McBride[1]

AFFILIATIONS

[1]Nuclear Engineering and Radiological Sciences, University of Michigan, Ann Arbor, Michigan 48109, USA
[2]Sandia National Laboratories, Albuquerque, New Mexico 87185, USA
[3]Laboratory of Plasma Studies, Cornell University, Ithaca, New York 14853, USA

[a]Author to whom correspondences should be addressed: jeffwool@umich.edu

ABSTRACT

Cylindrical foil liners, with foil thicknesses on the order of 400 nm, are often used in university-scale Z-pinch experiments ($\sim$1 MA in 100 ns) to study physics relevant to inertial confinement fusion efforts on larger-scale facilities (e.g., the magnetized liner inertial fusion effort on the 25-MA Z facility at Sandia National Laboratories). The use of ultrathin foil liners typically requires a central support rod to maintain the structural integrity of the liner target assembly prior to implosion. The radius of this support rod sets a limit on the maximum convergence ratio achievable for the implosion. In recent experiments with a support rod and a pre-imposed axial magnetic field, helical instability structures in the imploding foil plasma were found to persist as the foil plasma stagnated on the rod and subsequently expanded away from the rod [Yager-Elorriaga *et al.*, Phys. Plasmas **25**(5), 056307 (2018)]. We have now used the 3D extended magnetohydrodynamics simulation code PERSEUS (which includes Hall physics) [C. E. Seyler and M. R. Martin, Phys. Plasmas **18**(1), 012703 (2011)] to study these experiments. The results suggest that it is the support rod that is responsible for the helical structures persisting beyond stagnation. Furthermore, we find that as the radius of the support rod decreases (i.e., as the convergence ratio increases), the integrity and persistence of the helical modes diminish. In the limit with no support rod, we find that the structure of the final stagnation column is governed by the structure of the central precursor plasma column. These simulation results and their comparisons to experiment are presented.

Published under license by AIP Publishing. https://doi.org/10.1063/5.0012170

I. INTRODUCTION

Magnetized liner inertial fusion (MagLIF)[1,2] uses the 100-ns, 18- to 30-MA Z machine at Sandia National Laboratories to implode a thick-walled cylindrical metal tube (or "liner") onto a preheated and premagnetized fusion fuel (deuterium or deuterium–tritium). A typical MagLIF liner has an initial radius of about 3 mm, a wall thickness of about 0.5 mm, and a height of about 10 mm. The liner implosion is driven by the fast Z-pinch process[3] where the Z machine's current pulse is driven through the liner in the axial direction, with a current density J_z. This results in an azimuthal magnetic field B_θ and thus a $\mathbf{J} \times \mathbf{B}$ force density that is directed radially inward, which drives the implosion. The implosion is unstable to the acceleration-driven Magneto-Rayleigh–Taylor (MRT) instability[4–17] and to magnetic-compression-driven instabilities such as the $m = 0$ "sausage mode," the $m = 1$ "kink mode," and general $m \geq 1$ helical modes, where m is the azimuthal mode number,[18–20] which generally represents the

number of intertwined helices. These are fast-growing instabilities that are detrimental to implosion uniformity and thus to efforts in magnetically driven Inertial Confinement Fusion (ICF).[1,2,8,18–23]

In MagLIF, both the fuel and the metallic liner surrounding the fuel are premagnetized with an axial magnetic field B_z to limit thermal conduction losses from the hot fuel to the cold liner. From penetrating radiography experiments on the Z-machine at Sandia National Laboratories, the combination of the premagnetizing B_z field with the implosion-driving B_θ field was found to result in helical instability structures with $m \approx 6$.[23] Furthermore, when $B_z = 0$, these helical modes are absent, and the instability structures become azimuthally correlated.[6,24] The development of the helical modes for $B_z \neq 0$ was surprising because B_θ was expected to quickly dominate over B_z since B_θ grows rapidly as the current on Z surges to $\sim$20 MA, while B_z was expected to stay roughly constant, at its initial value of about 10 T. As the fastest growing modes of MRT satisfy $\mathbf{k} \cdot \mathbf{B} = 0$, seeing helical

modes suggests that B_z was large enough to make B_z/B_θ significant. Additionally, at the time of the original experiments with $B_z \neq 0$, computer simulations had not predicted the formation of helical instability structures.

The formation of helical instability modes in liner implosions is still a subject of debate, but it has been studied extensively in recent years in both simulation[25] and experiment.[9,18] For example, Seyler et al. recently published a numerical simulation study,[25] which appears to support the explanation proposed by Ryutov et al.,[4] where low-density plasma around the liner is swept radially inward by the driving B_θ field, compressing the axial magnetic flux entrained in the plasma up against the liner's outer surface, which increases the strength of B_z at the liner's outer surface. This also increases the ratio of B_z/B_θ at the liner's outer surface relative to the case with no flux compression of the B_z field. With a high enough B_z/B_θ ratio, helical modes could be driven.

The numerical study by Seyler et al.[25] used the PERSEUS simulation code,[26] which was developed at Cornell University. PERSEUS is a fully three-dimensional extended magneto-hydrodynamics (XMHD) code that includes Hall physics and is capable of handling a plasma density range of approximately eight orders of magnitude. The ability to include Hall physics is key to the formation of helical instabilities in the code as it allows for more robust handling of plasma densities as low as 10^{14} cm^{-3}. Simulating the formation of these helical instabilities on the liner has been challenging for many MHD codes in the past. For example, resistive MHD codes have been unable to capture these helical instability structures without deliberate helical seeding from the user,[8,23] or artificially enhancing the pre-imposed axial magnetic field. By contrast, PERSEUS is able to produce helical instabilities with the use of Hall physics, with no need for initial helical seeding. The possible mechanisms for this are discussed in Seyler et al.,[25] but may require further exploration in a future paper.

To study metal liner implosion instabilities on a university-scale pulsed power machine ($\sim$1 MA in 100 ns) requires a significant reduction in the liner wall thickness relative to MagLIF liners on Z. Thinner liner walls are needed to reduce the overall liner mass while preserving the initial liner radius of 3 mm. Thin liner walls can be achieved by wrapping a sheet of thin metal foil (e.g., 400-nm-thick aluminum) into the shape of a cylinder. Thin-foil liners of this type have been used in experiments on the MAIZE facility at the University of Michigan[18–20,27,28] and the COBRA facility at Cornell University.[29,30] Because the foil liners are so thin, they are also incredibly fragile and require a support rod structure (Fig. 1) to ensure their structural integrity when handling (e.g., during liner assembly and installation into the MAIZE anode–cathode structure), as well as during vacuum pump-down on MAIZE, where the gap spacing of the anode–cathode structure can decrease by $\sim$1 mm in the axial direction of the liner as the MAIZE facility's plastic insulators compress due to the 1 atm pressure differential. In Fig. 1, the dumbbell-shaped support rod structure is shown both with and without the foil liner wrapped around the structure.

The development of an imploding thin-foil liner platform on MAIZE enabled subsequent experimental studies on liner implosion dynamics. These studies included experiments with axially premagnetized liners, where discrete helical modes were observed.[18–20] In thin-walled foil liner experiments[20] and in thick-walled MagLIF liner experiments,[23] the helical pitch angle φ and the azimuthal mode
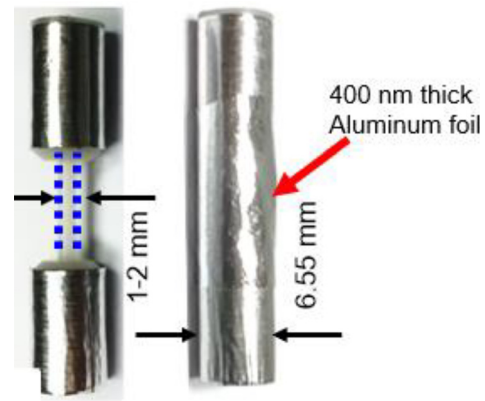

FIG. 1. Support rod structure needed to handle ultrathin foils during installation and vacuum pump down on MAIZE. This structure was used in the experiments of Refs. 18–20 and 27. The effects of this structure are explored in this paper.

number m of the helical instability structures were found to be governed by the strength of the initial applied B_z field. Additionally, the pitch angle in both the thin- and thick-walled cases can be described by the relationship $\varphi \approx m/(kR)$, where k is the axial wave number, and R is the imploding liner radius at the time of the image, while the helical pitch $p = 2\pi m/k$ was found to be approximately constant in both the thin- and thick-walled cases for the implosion times observed.[20,23] (Note that the helical pitch is the axial distance traveled along a helix when advancing by 2π radians in the azimuthal direction; the pitch is not the pitch angle.) The similarities observed between the two cases are remarkable given that thin-foil liners are much more susceptible to instability feedthrough than thick-walled MagLIF liners. For example, a liner's robustness to instability feedthrough is often characterized in terms of the liner's initial aspect ratio $AR_0 \equiv R_{outer,0}/\Delta R_0$, where $R_{outer,0}$ is the initial radius of the liner's outer surface, and ΔR_0 is the liner's initial wall thickness. Smaller AR_0 liners are expected to be more robust than higher AR_0 liners, while higher AR_0 liners can obtain higher implosion velocities. In MagLIF, the tradeoff between implosion velocity and liner stability is expected to result in optimum fusion performance with $AR_0 \sim 6$ liners, which have been studied extensively on Z.[6,9,23] By contrast, the thin-foil liners studied in Refs. 18–20 and 28 have $AR_0 \sim 6000$. Another important difference between the thin- and thick-walled cases is the fact that the wall thickness in a MagLIF liner is usually greater than the electrical skin depth of the liner material, whereas in thin-foil liner experiments, the resistive skin depth is much greater than the liner wall thickness. This causes thin-foil liners to explode (expanding the wall thickness) very early in the current pulse, due to the stresses caused by intense ohmic heating. By contrast, MagLIF liner walls are usually compressed by the driving magnetic pressure gradient, sometimes leading to shock formation within the thick liner wall.[24] For the thin-foil liner experiments, the early expansion of the foil thickness prior to the start of the implosion effectively reduces the initial aspect ratio to $AR_{0,effective} \sim 15$, which could help explain some of the similarities observed between initially thin- and thick-walled cases.

In this paper, we present results from PERSEUS simulations of the thin-foil liner experiments described in Refs. 18–20. These

simulations were performed using 64 cores on the University of Michigan's FLUX computing cluster, where over 7 million cells were simulated, requiring upward of 60 wall clock hours per simulation. The spatial resolution (cell size) was approximately 73 μm $\times$ 73 μm $\times$ 62.5 μm, and the simulation volume was approximately 14 mm $\times$ 14 mm $\times$ 12 mm. A random density perturbation of less than 1% was applied to the liner cells to seed instabilities. Such a small perturbation was chosen to minimize the influence of the seed while still causing instabilities to grow. As mentioned above, PERSEUS is able to produce helical instabilities with the use of Hall physics, with no need for initial helical seeding by the user.[25] Here, we attempt to validate the helical modes generated by PERSEUS by comparing the PERSEUS results with the experimental results presented in Refs. 18–20. Results from this numerical study with PERSEUS suggest that the on-axis support rod plays a key role in the persistence of helical modes post-stagnation. Furthermore, we find that as the radius of the support rod decreases (i.e., as the convergence ratio increases), the integrity and persistence of the helical modes diminish. In the limit with no support rod, we find that the structure of the final stagnation column is governed by the structure of the central precursor plasma column. These simulation results and their comparisons to experiments are presented throughout the remainder of this paper.

II. SIMULATIONS OF PREVIOUS EXPERIMENTS CONDUCTED ON MAIZE

Liner implosions, like those studied experimentally in Refs. 18–20, can be described as having four phases: (1) an ablation phase, (2) an implosion phase, (3) a stagnation phase, and (4) an explosion phase. The ablation phase is particularly challenging to model. For example, advanced conductivity and equation-of-state (EOS) models are needed to accurately describe the liner material as the liner transitions from the solid state to a liquid-vapor state to a variably ionized plasma state. For the studies reported here, however, PERSEUS was only equipped with a Spitzer–Harm conductivity model and an ideal gas equation of state. Additionally, due to limitations in computing resources, it was not practical to resolve the ablation of an ultrathin (400-nm-thick) liner. Thus, to set the initial conditions in our 3D PERSEUS simulations, we made use of 1D HYDRA simulations conducted specifically to study foil ablation dynamics.[31] We used the HYDRA results as a guide to initialize our PERSEUS simulations 50 ns into the current pulse (i.e., we did not have access to the HYDRA simulation data; thus, we were unable to import the HYDRA data directly into PERSEUS). By 50 ns, the liner already ablated and expanded into a ~250-μm-thick plasma that is ~1 eV in temperature, which PERSEUS is then better able to handle. The density and temperature spatial distributions in the liner shell were initialized to be uniform, with the exception of the less than 1% random density perturbation mentioned in Sec. I. We note that the plasma velocity at 50 ns is relatively close to zero, because this is the end of the ablation phase and prior to any implosion; thus, the plasma velocity was initialized to zero. Along with the liner parameters, we also initialized the driving magnetic field, B_θ, for $r > r_{outer}$. Despite initializing B_θ exclusively outside the liner, the magnetic field quickly diffuses through the liner wall, within approximately 5 ns of the start of the PERSEUS simulation (i.e., during the period of 50–55 ns into the current pulse). Note that the current is still relatively low during this period (~100 kA). As the current rises to >500 kA, the plasma temperature

rises to ~100 eV, causing the plasma conductivity to increase, which decreases the magnetic diffusion rate through the liner wall. Once the implosion starts, approximately 30% of the total load current has diffused through the liner wall and is present in the region between the support rod and the liner.

An overview of the initial 3D PERSEUS simulation geometry and some example images of the imploding liner plasma are presented in Fig. 2. As in the experiments, the simulations included a pre-imposed axial magnetic field of 2 T. The liner plasma density was mass matched to represent a 400-nm-thick aluminum foil liner expanded out into a ~1 eV cylindrical plasma shell with a wall thickness of 250 μm. The random density perturbation of less than 1% was distributed throughout the liner plasma. PERSEUS was also modified to read in an experimentally measured current pulse to drive the implosion (see Fig. 3).
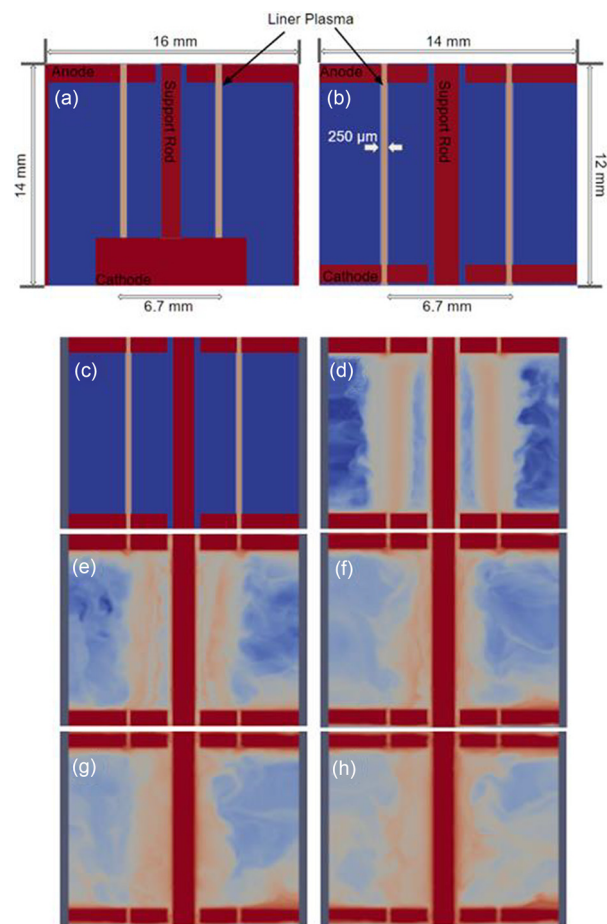

FIG. 2. Simulation setups and implosion overview. (a) and (b) Initial setups showing examples of the electrode geometries and power feeds used. The setup in (a) includes an axial feed and was driven by a boundary condition at the lower edge of the image (i.e., at a specified axial position). The setup in (b) used a simplified electrode geometry and was driven by a boundary condition at the left and right edges of the image (i.e., at a specified radius). It was found that including the axial feed was unnecessary and only added unnecessary volume to the simulation space, forcing us to reduce grid resolution; thus, the setup in (b) was used for most of this paper. (c)–(h) Example density slices taken during a representative liner implosion.
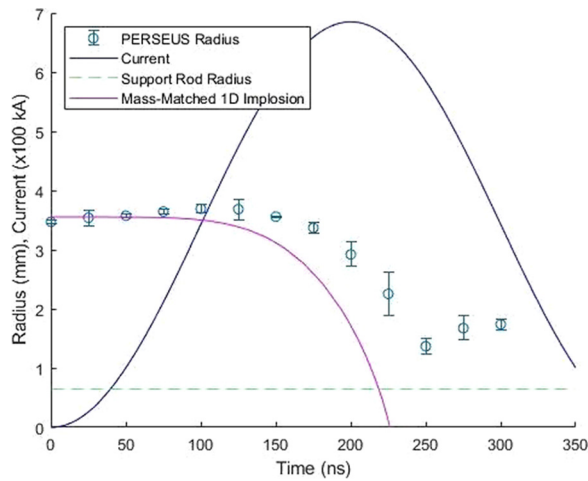
FIG. 3. Simulated liner implosion trajectories from PERSEUS and from a simplified 1D thin-shell model, as well as the MAIZE electrical current used to drive the simulated implosions. This figure should be contrasted with Fig. 1(b) in Ref. 19. The simplified 1D thin-shell simulation (sometimes referred to as a "0D" model) is shown for reference and demonstrates that PERSEUS captures early time expansion of the liner and late time bounce of the liner off of the inner support rod, which can also be seen in experiment [Fig. 1(b) in Ref. 19].

The PERSEUS implosion trajectory presented in Fig. 3 was extracted from the simulation data presented in Fig. 2. To obtain the PERSEUS radii plotted, several 1D radial density profiles were acquired by taking radial lineouts through the 3D simulation data at various axial positions (z) and azimuths (θ). The outer edge of each radial profile was then recorded. The averages (means) of these positions are the PEREUS radii plotted in Fig. 3, while the standard deviations are the error bars plotted.

At present, PERSEUS only allows for a single material to be modeled. Thus, to model both the imploding aluminum plasma shell and the plastic support rod, the support rod was initialized as cold, solid-density aluminum with its conductivity artificially decreased so that it was non-conducting. A momentum mask (which prevented any movement of the rod due to thermal expansion or ablation by artificially imposing zero momentum at every timestep while active) was also applied to the rod during the liner implosion phase and then removed at a time just before liner stagnation. This was done to prevent rod ablation from impacting the inner surface of the imploding liner. To mimic the ionization of the rod's surface, a thin (2-cell) layer of low-density plasma was initialized around the rod. This allowed for the flow of a small amount of current along the rod's surface. It is difficult to know the exact behavior of the rod since it has not been explored in experiment, but we believe this approach to be reasonable and sufficient for the purposes of this study.

In Fig. 3, the PERSEUS liner trajectory reaches stagnation just after the time when the current reaches its maximum value. The stagnation phase begins when the liner begins to decelerate due to plasma pressure building up between the imploding liner wall and the support rod on axis. During stagnation, the liner trajectory appears to undulate. This is due to shocks reverberating in the plasma between the imploding liner wall and the support structure on axis. After stagnation, the liner trajectory enters the explosion phase. In Fig. 3, the

duration of the implosion phase is approximately 125 ns, and the duration of the stagnation phase is approximately 50 ns. These durations are in good agreement with those observed experimentally in Fig. 1(b) of Ref. 19.

In our PERSEUS simulations, and in the experiments of Refs. 18–20 and 27, the on-axis support rod sets a maximum possible convergence ratio of $C_{r,max} \equiv \frac{r(0)}{r_{rod}} = 5.15$. However, this $C_{r,max}$ is never achieved in the simulations or observed in the experiments (note that the experiments only observed the outer edge of the imploding liner plasma). At least for the simulations (and possibly for the experiments), this is due to an appreciable amount of low-density plasma being advected to the support rod ahead of the bulk of the imploding liner material. This advected "precursor" plasma accumulates along the rod while also carrying an appreciable amount of current ($\sim$30%). This precursor plasma, with its associated plasma pressure and magnetic pressure, is compressed by the imploding liner material, which limits the convergence ratio to something less than $C_{r,max}$. This is discussed in greater detail in Secs. III and IV.

Overall, the simulated trajectory in Fig. 3 is very similar to that found in the experiments of Ref. 19 [see Fig. 1(b) in Ref. 19]. However, one notable difference is that the liner begins imploding earlier in the simulated case (both PEREUS and the simple thin-shell model). In experiments, the liner began the implosion phase around 125 ns into the current pulse, while in PERSEUS, the liner begins the implosion phase around 75 ns into the current pulse. This results in the PERSEUS liner reaching stagnation earlier than in the experimental case. This discrepancy could be due to the use of a Spitzer–Harm conductivity model, which lacks the ability to model the precipitous drop in conductivity that occurs when the solid metal foil transitions to a liquid–vapor state. By artificially varying the conductivity values, we found that the implosion timings could be varied by 10s of nanoseconds, where higher conductivity values lead to earlier implosion times, because larger gradients in the implosion-driving magnetic field pressure can be supported. The conductivity values were varied through a weighting factor that determines the relative weight of a fixed conductivity value versus a value calculated using the Coulomb logarithm. From these two values, an overall conductivity value for each cell is calculated. Efforts are presently underway to improve the conductivity models in PERSEUS and thus further address this discrepancy in the future.

Another possible explanation for the discrepancy in the overall implosion times is that, perhaps, the current delivered to the load in the experiments was lower than the measured value. For example, the load current diagnostics in the experiments of Refs. 18–20 were B-dot probes located at a radius of 45 cm, which is large compared to the radius of the liner (3 mm). This means that any current loss occurring between the probe locations and the liner surface would go undetected while also causing a later-than-expected implosion time, given the measured current trace. To test this explanation, we ran a simple PERSEUS simulation and found that lowering the current by 15% caused the liner to implode $\sim$25 ns later. Furthermore, in the experiments of Ref. 19, the peak current varied from shot to shot by up to 20% of the average peak current measured. Meanwhile, our PERSEUS simulations used the current trace from the experiment with the highest peak current (shot 1172, with a peak current of 680 kA). Thus, the shot-to-shot variations and the measurement uncertainties could explain much of the differences observed in the implosion times.
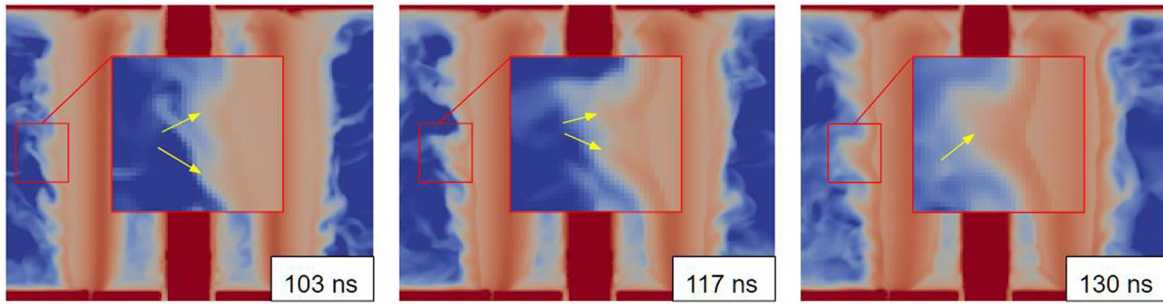
FIG. 4. Mode merging of instability lobes in simulation. The duration of this single mode-merging event is approximately 30 ns. Both the duration and the overall dynamics of this mode-merging event agree well with the experimental results presented in Fig. 7(b) of Ref. 20.

We note that efforts are presently underway to improve load current measurements on MAIZE and thus further address this issue in the future.[32] Despite the discrepancy in the start time of the implosion phase, we emphasize that the simulated durations of the implosion and stagnation phases are in good agreement with the experiment.

During the implosion phase, instability structures begin to develop. Considering the axial mode number (spatial frequency) $k_z = 2\pi/\lambda$, where λ is the wavelength of the instability in the axial direction, the first modes to appear are short-wavelength modes (high spatial frequency), which cascade to larger wavelength modes throughout the implosion.[6,20] This cascading process occurs via a series of discrete mode merger events.[20] The discrete mode merger events observed in the PERSEUS simulations (see Fig. 4) appear very similar to those observed in experiments [see Fig. 7(b) in Ref. 20]. In both the simulation and in the experiment of Ref. 20, the discrete merging of two instability lobes occurs over a period of approximately 30 ns.

As the instability structures cascade to longer wavelengths, they also grow to larger amplitudes.[6,20] In Fig. 5, the PERSEUS instability
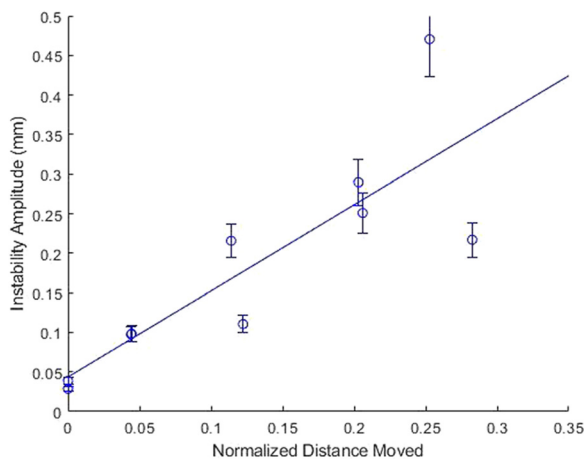

FIG. 5. PERSEUS-simulated instability amplitude as a function of the normalized distance moved, $\hat{d} \equiv 1 - r(t)/r(0)$. The instability amplitude is subject to the iso-density surface chosen and becomes difficult to determine as the liner begins to bounce off of the inner support rod. This is due to the lowering resolution as the liner moves through the cartesian grid, which can make it difficult to determine a precise instability amplitude.

amplitude is presented as a function of the normalized distance moved, $\hat{d} \equiv 1 - r(t)/r(0)$. To obtain these amplitudes, we tracked the edge of the imploding plasma column and fit a sum of sine functions to the plasma edge (fit function made using Matlab "sin8" fitting routine). This allowed us to determine an average instability amplitude for each time step that was analyzed. The amplitude data were then fit with an exponential function of the form $A = A_0 \exp(\gamma t)$, where A_0 is determined by the initial seeding and γ is the growth rate. Since a random density perturbation was used in these simulations, A_0 was not well defined (i.e., this is a perturbation to density rather than a perturbation to the liner–vacuum interface). Nevertheless, the exponential fits allow us to determine the growth rates and an *effective* A_0. The PERSEUS growth rate found was $34.5 \pm 5.5\ \mu s^{-1}$, which was a factor of ≈ 3 times larger than the experimentally measured values, which typically ranged from 7 to 13 μs^{-1}. However, because the simulated liners were imploding while the experimental liners were non-imploding (to investigate the magnetic compression instability development in a case that is decoupled from the acceleration-driven MRT instability), it is not surprising that the overall instability growth rates in our PERSEUS simulations (which do include MRT contributions) are larger than in the experiments of Ref. 20. The uncertainty in our simulated growth rate is largely due to limitations in spatial resolution. The lack of resolution causes aliasing to occur (on a Cartesian grid) that influences the measured growth rate at different azimuthal locations on the liner. This means that the measured growth rate can depend on the azimuthal viewing angle. Viewing angle effects are also caused by mode merger events occurring at different azimuths at different times. In simulations, the effects of the viewing angle can be mitigated by rotating the 3D data such that the chosen viewing angle for data analysis takes into account the azimuthally asymmetrical mode merger events. This is not possible in experiment; thus, viewing angle effects may play a more significant role there.

In Fig. 6, simulation results are presented that reveal an axial asymmetry in the instability structure. Specifically, the instability structure curls upwards in a way that is similar to a Kelvin–Helmholtz instability. This effect has also been observed in wire-array Z-pinch experiments.[33,34] This wavelike curl is due to the $\mathbf{E} \times \mathbf{B}$ drift of the plasma from the radial electric field and the azimuthal magnetic field, which causes the plasma at the outer tips of the instability lobes to drift upwards and curl over like a breaking wave. This curled up axial asymmetry, combined with the helical pitch angle of the instability structure for simulations with $B_z \neq 0$, complicates the process of accurately

extracting an instability amplitude from the simulation data. These combined instability structures (i.e., the curled up axially asymmetric structure and the helical structures) can also enhance the differences perceived in the overall instability amplitude when viewing the liner from different azimuthal angles.

Helical modes were observed in all simulations run with $B_{z0} \neq 0$ (see Fig. 7). To characterize these modes, we used the analysis technique presented by Awe et al.,[23] where the observed helical structures can be fit using the parametric equations: $y(\theta) = a^*\sin(\theta)$, and $z(\theta) = p*\theta/2\pi$. Here, a is the radius of the imploding liner at the time of the image, and p is the pitch of the helix. Note that p remains approximately constant throughout the implosion, which is consistent with the fact that axial plasma outflows are not permitted in the experiments or the simulations. In Fig. 7(a), we show a series of helical lobes highlighted on the surface of the liner (an iso-density surface taken at a number density of 6×10^{18} cm^{-3}). In Fig. 7(b), we show the corresponding helical traces from the parametric equations above; these parametric fits are used to identify the effective azimuthal mode number.

The choice of the iso-density surface was made such that the instability structures were the most pronounced. This typically meant a surface of 6×10^{18} cm^{-3}. Changing this value by an order of magnitude higher or lower does not affect the results presented in this paper. We note that if the density threshold for the iso-surface is set too low, then random clumps of low-density plasma begin to obscure a decent view of the helical structures, while if the density threshold is set too high, the structures are not present.

The parametric fitting technique is able to trace well-defined helical lobes, but it does not handle the more complex structures that result from the discrete mode merging events that occur at different azimuths at different times. Nevertheless, we include this simplified tracing method to capture the general trends of the mode development and to give a rough idea of the effective azimuthal mode number (i.e., the number of intertwined helices), which we were able to confirm by rotating our 3D data. The results from this analysis for six different times can be seen in Fig. 8. Late in time, the modes become less pronounced as the plasma becomes denser, and choosing an optimal iso-density surface becomes more challenging. We see from these traces that the number of intertwined helices early in time is quite large (m ≈ 7) compared to the final number at stagnation ($m \approx 2$). We can also see from this analysis that one helical trace can become very close to another helical trace (see Fig. 7), which is a consequence of
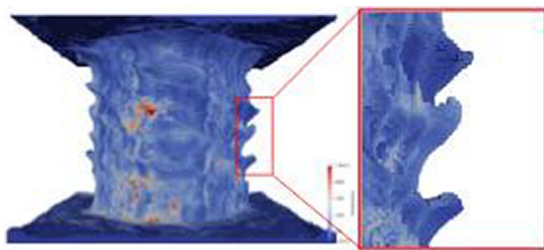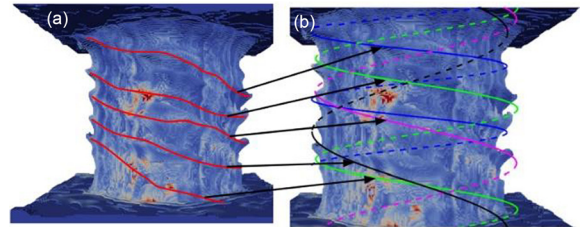

FIG. 7. Iso-density surface images taken at a number density of 6×10^{18} cm^{-3} and a time of 117 ns, showing (a) the highlighted helical instability lobes that develop on the liner and (b) the corresponding helical line traces used to identify the effective azimuthal mode number. The origin of these helical instabilities is being studied and will be presented in depth in a future paper.

instability lobes being in the process of merging (Fig. 4). Also note that since the helical modes are almost always in a state of merging, the effective azimuthal mode number is rarely (if ever) an exact integer value, hence the uncertainties indicated in Fig. 8. We note that the experimental data of Refs. 18–20 were acquired using laser shadowgraphy (with a laser wavelength of 532 nm) and visible self-emission imaging. A straightforward way to compare the PERSEUS simulation results to the experimental results would be to use PERSEUS simulation output data to generate synthetic laser shadowgraphs and self-emission images. However, PERSEUS is presently not equipped to do this. Synthetic diagnostics in PERSEUS is presently a work-in-progress.

The origin of these helical modes in our thin-foil liner simulations is still a topic of ongoing research. In our simulations, we do not seed a low-density plasma in the A–K gap as was done for the
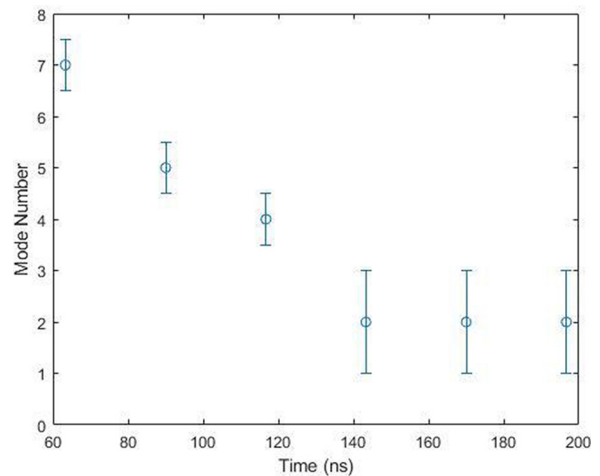

FIG. 8. Effective Azimuthal mode number m as a function of time. The mode numbers were extracted from the simulation data using the helical fitting technique described by Awe et al. in Ref. 21. This technique uses the parametric equations given in the text to trace 3D helices onto a 2D image. The results plotted here indicate that the instability structure initially consists of many intertwined helices ($m \approx 7$) and that these helices merge into fewer helices throughout the implosion process. The mode merging ceases upon stagnation ($t \approx 140$ ns), with a dominant mode number of $m \approx 2$ (two intertwined helices). These results are consistent with the experimental results presented in Refs. 18–20.

FIG. 6. Simulation showing the curled-up wavelike structure of the instability lobes, which develops during the rising edge of the current pulse due to an upward-directed **E** × **B** drift. For an experimental comparison, see Figs. 1(b) and 1(c) in Ref. 33.

thick-shell MagLIF simulations by Seyler et al.,[25] because we do not believe that there was a significant amount of plasma in the A–K gap of the MAIZE experiments[19,20] with which we are comparing. In fact, experiments are presently underway on MAIZE to examine how electromagnetic power flow is affected by low-density plasma in the A–K gap, and it was found to be necessary to provide an auxiliary source of plasma in the A–K gap to have a detectable amount of plasma present in the A–K gap.[35] Furthermore, in our simulations, the amount of flux compression observed is much less than that seen in the MagLIF simulations of Seyler et al.[25] What we do know is that Hall physics is the driver for the helical instabilities observed in the PERSEUS simulations, as helical instabilities are not observed when Hall physics is removed from the simulation. We are currently exploring this further and believe that a Hall instability[36–38] provides the mechanism for generating the helical instabilities in these thin-foil liner implosions. This work will be presented in a future publication.

III. SUPPORT ROD DIAMETER EFFECTS ON HELICAL MODE PERSISTENCE

In the past experiments where a thin-foil liner implosion was pre-magnetized with a uniform externally applied B_z field, it had been observed that helical modes developed during the implosion phase and persisted into the explosion phase.[19,20] These experiments included an on-axis support rod (Fig. 1). In our initial modeling attempts, we did not include this on-axis support rod, and we did not observe the persistence of helical modes during stagnation or during the subsequent explosion phase. This led to the hypothesis that the persistence of the helical modes into the explosion phase was caused by the support rod limiting the convergence ratio of the implosion. We then tested this hypothesis by including a support rod in our simulations and found that, indeed, the helical structures remained intact into the explosion phase, after bouncing off of the support rod. To find the point where the support rod took effect (i.e., to find the maximum convergence ratio where helical structures persist), four cases were simulated: an implosion with a support rod radius of 0.50 mm, 0.25 mm, and 0.10 mm, as well as a case with no support rod. In each case, helical instabilities form during the implosion phase as expected. During the explosion phase, however, differences were noted. To compare each case, the plasma column at 10 ns post-stagnation is presented in Fig. 9.

For each case, an iso-density surface was chosen at 1×10^{19} cm^{-3} and then color contrasted so that the plasma structures on the liner could be more easily identified. The instability structures are then traced and highlighted in Fig. 9 to more clearly show the differences in each of the four scenarios. Figure 9(a) shows that with a support rod of 0.5 mm, the helical structures are preserved past stagnation, which is consistent with the experimental results of Ref. 20. Figure 9(d) shows that with no support rod, the helical structure is almost entirely lost. There appears to be little-to-no difference between Figs. 9(c) and 9(d), indicating that a support rod radius of 0.1 mm has little-to-no effect on preserving the helical structures post stagnation. Figures 9(a)–9(c) show that the helical structure is increasingly preserved as the support rod radius is increased.

In Fig. 10, we include a more detailed time evolution comparison of the case with a support rod of radius = 0.5 mm [Fig. 10(a)] and the case with no support rod [Fig. 10(b)]. In each case, there are clear helical structures at peak current (labeled as "+0ns"), but as the liners
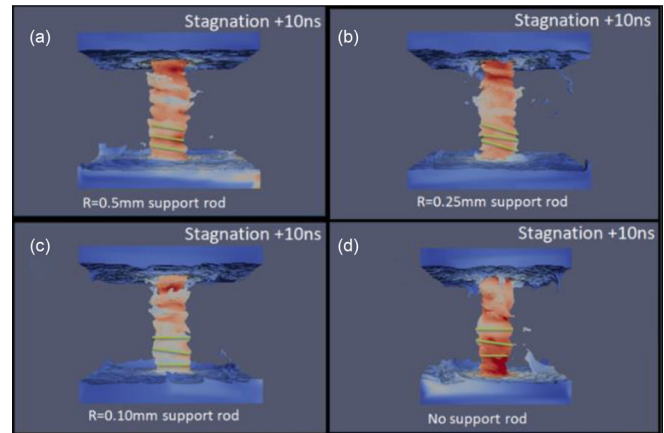

FIG. 9. Comparison of thin-foil implosions for four different cases of on-axis support rod radii: (a) 0.5 mm, (b) 0.25 mm, (c) 0.1 mm, and (d) 0 mm (no rod). The time chosen for this comparison is 10 ns after stagnation. The iso-density surface shown is 1×10^{19} cm^{-3}. The image in part (a) should be contrasted with Fig. 5 in Ref. 20.

reach stagnation and then expand outward, the helical structures are preserved in the explosion phase of the case with the support rod and not in the case with no support rod. For ease of comparison, we colored the plots in Fig. 10 by distance from the axis so that the differences in structure are more apparent past stagnation.

For the case with no support rod, a plasma column forms on axis from low-density "precursor" plasma being blown in ahead of the bulk of the imploding liner material. The morphology of the on-axis precursor plasma, prior to the arrival of the bulk of the imploding liner material, has been found to set the morphology of the final bulk stagnation column in wire-array Z-pinch experiments[39] as well as in our thin-foil liner simulations. A more detailed analysis of this behavior is presented in Sec. IV. For now, we simply note that the addition of a massive on-axis support rod prevents this relatively low-density precursor plasma from morphing into a shape other than that of the much more massive on-axis support rod. Instead, the precursor plasma accumulates along the smooth surface of the support rod, creating a uniform cushion for the bulk of the liner material to implode onto. This cushion, along with the rod radius, dictates the maximum convergence ratio that the imploding liner will obtain.

The maximum convergence ratio achieved in each of the four cases is listed in Table I. Because of the instability structure, it is difficult to determine the minimum radius achieved by the liner at stagnation. To determine a minimum radius and thus a convergence ratio, each of the four cases was analyzed at the point of stagnation as follows. Only the plasma of density equal to or greater than the initialized liner density of 6×10^{19} cm^{-3} was considered. This is plasma three orders of magnitude less than solid density. Plasma of density below this threshold was ignored. Next, the average radius of this plasma column was determined by measuring the radius of each instability peak and trough along one side of the plasma column. These values were then averaged to obtain an approximate average radius of the column. Referring to Table I, the convergence ratio does not vary strongly with the radius of the support rod for support rod radii of 0.25 mm and smaller. Furthermore, the convergence ratio for the 0.5-mm case is notably smaller than that of the other three cases. The 0.5-mm case is
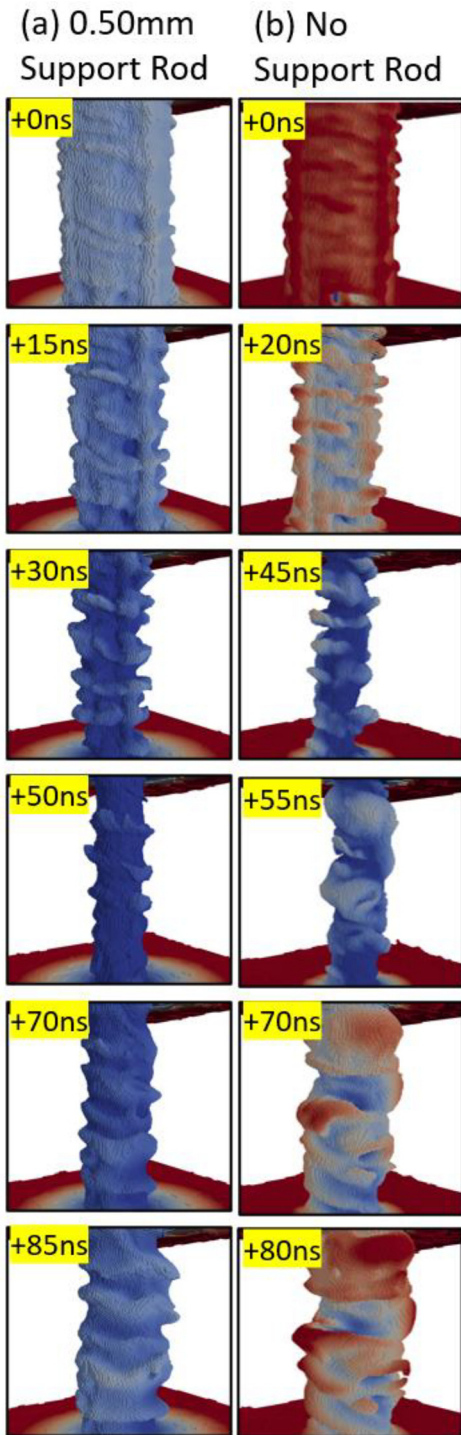
FIG. 10. Time evolution comparison of thin-foil implosions for on-axis support rod radii of (a) 0.5 mm and (b) 0 mm (no rod). The time labels are relative to peak current. For ease of contrasting, the coloring is based on the distance from the cylindrical axis and is tinted slightly red for the case with no support rod and slightly blue for the case with the support rod. The iso-density surface shown is 1 × 10^{19} cm^{-3}.

TABLE I. Minimum radius and maximum convergence ratio obtained for each of the four support-rod cases simulated.

Support rod radius (mm)	Average radius at stagnation (mm)	Convergence ratio (Cr)
0.5	1.045	2.87
0.25	0.62	4.84
0.1	0.791	3.79
0	0.756	3.95

also the case where helical instability structures were best preserved after stagnation.

IV. PRECURSOR PLASMA COLUMN MORPHOLOGY

Without a support rod, a precursor plasma column is able to form from plasma blown in ahead of the imploding liner bulk. This precursor plasma column sets up on axis early in time, before the bulk of the imploding liner material stagnates on top of it. In our PERSEUS simulations, the morphology of the precursor column determines the morphology of the final stagnation column. This is shown in Fig. 11, where we highlight the formation of structures in this central plasma column that then develop into the dominant structures of the stagnating and exploding plasma bulk. In Fig. 11, the formation of a well-defined plasma structure in the precursor and stagnation columns is highlighted by the white arrow. Similar behavior has been observed previously in wire-array Z-pinch experiments [see Fig. 13(b) in Ref. 39]. Although precursor plasma columns are often observed in wire-array Z-pinch experiments, they are more difficult to observe in liner implosion experiments because the imploding liner wall obscures a direct side-on view of the precursor plasma for most diagnostics
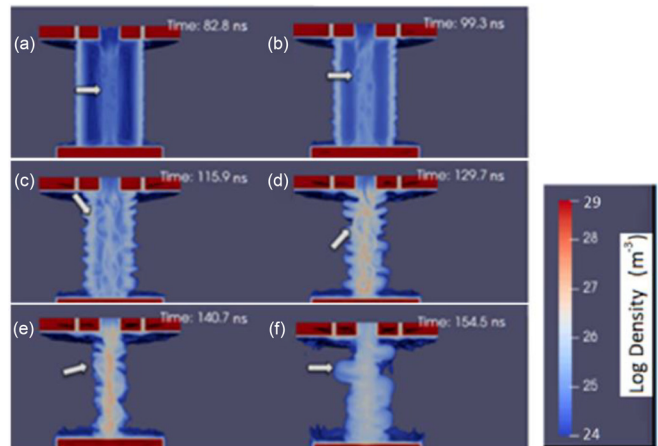

FIG. 11. Simulation of a thin-foil liner implosion with no support rod on axis. The lack of a support rod allows a precursor plasma column to assemble on axis with various instability structures. A particularly well-defined structure is identified by the white arrow. This structure is tracked through stagnation and into the explosion phase. These six frames illustrate that the morphology of the low-density precursor plasma, which arrives on axis ahead of the imploding liner bulk, is largely responsible for setting the morphology of the imploding liner bulk during stagnation and explosion. This figure should be contrasted with Fig. 13(b) in Ref. 39.

(i.e., non-penetrating diagnostics). Nonetheless, precursor plasmas in metal liner experiments have been detected by inserting B-dot probes inside the imploding liner.[24] They can also be imaged using end-on diagnostics.[40] Though a detailed discussion of wire-array Z-pinch physics is beyond the scope of this paper, we note that the physics of wire ablation and precursor plasma formation in wire-array Z-pinches is a bit different from the precursor plasma formation in thin-foil liner experiments. Nevertheless, the fact that PERSEUS appears to capture the physical connection between the morphology of the precursor plasma column and the morphology of the stagnation column, as has been observed in wire-array Z-pinch experiments,[39] is encouraging.

V. SUMMARY

In this paper, we have shown that PERSEUS is able to capture dominant plasma features in imploding liners, such as mode merging in helical instability structures (Fig. 4) and wavelike instability structures that curl over in the $\mathbf{E} \times \mathbf{B}$ direction (Fig. 6). Quantitatively, we have shown that the effective azimuthal mode number starts off relatively high ($m \approx 7$ at the start of the implosion) and through discrete mode merger events, drops to a final constant value of $m \approx 2$ during stagnation and explosion (Fig. 8). We have shown that the persistence of helical structures into the explosion phase depends on having an on-axis support rod with a large enough radius (≈ 0.5 mm) to significantly limit the convergence ratio obtained at stagnation (Figs. 9 and 10). A larger support rod radius reduces the convergence ratio at stagnation, thereby better preserving the helical instability structures and the overall liner integrity. We also showed that a precursor plasma column forms in the case of no support rod and that the morphology of this precursor structure determines the morphology of the final stagnation column (Fig. 11).

ACKNOWLEDGMENTS

DATA AVAILABILITY

The data that support the findings of this study are available from the corresponding author upon reasonable request.

REFERENCES

[1]S. A. Slutz, M. C. Herrmann, R. A. Vesey, A. B. Sefkow, D. B. Sinars, D. C. Rovang, K. J. Peterson, and M. E. Cuneo, Phys. Plasmas **17**, 056303 (2010).

[2]M. R. Gomez, S. A. Slutz, A. B. Sefkow, D. B. Sinars, K. D. Hahn, S. B. Hansen, E. C. Harding, P. F. Knapp, P. F. Schmit, C. A. Jennings, T. J. Awe, M. Geissel, D. C. Rovang, G. A. Chandler, G. W. Cooper, M. E. Cuneo, A. J. Harvey-Thompson, M. C. Herrmann, M. H. Hess, O. Johns, D. C. Lamppa, M. R. Martin, R. D. McBride, K. J. Peterson, J. L. Porter, G. K. Robertson, G. A. Rochau, C. L. Ruiz, M. E. Savage, I. C. Smith, W. A. Stygar, and R. A. Vesey, Phys. Rev. Lett. **113**, 155003 (2014).

[3]D. D. Ryutov, M. S. Derzon, and M. K. Matzen, Rev. Mod. Phys. **72**, 167 (2000).

[4]D. D. Ryutov, T. J. Awe, S. B. Hansen, R. D. McBride, K. J. Peterson, D. B. Sinars, and S. A. Slutz, in AIP Conference Proceedings (2014), pp. 63–66.

[5]E. G. Harris, Phys. Fluids **5**, 1057 (1962).

[6]R. D. McBride, S. A. Slutz, C. A. Jennings, D. B. Sinars, M. E. Cuneo, M. C. Herrmann, R. W. Lemke, M. R. Martin, R. A. Vesey, K. J. Peterson, A. B. Sefkow, C. Nakhleh, B. E. Blue, K. Killebrew, D. Schroen, T. J. Rogers, A. Laspe, M. R. Lopez, I. C. Smith, B. W. Atherton, M. Savage, W. A. Stygar, and J. L. Porter, Phys. Rev. Lett. **109**, 135004 (2012).

[7]K. J. Peterson, D. B. Sinars, E. P. Yu, M. C. Herrmann, M. E. Cuneo, S. A. Slutz, I. C. Smith, B. W. Atherton, M. D. Knudson, and C. Nakhleh, Phys. Plasmas **19**, 092701 (2012).

[8]T. J. Awe, C. A. Jennings, R. D. McBride, M. E. Cuneo, D. C. Lamppa, M. R. Martin, D. C. Rovang, D. B. Sinars, S. A. Slutz, A. C. Owen, K. Tomlinson, M. R. Gomez, S. B. Hansen, M. C. Herrmann, M. C. Jones, J. L. McKenney, G. K. Robertson, G. A. Rochau, M. E. Savage, D. G. Schroen, and W. A. Stygar, Phys. Plasmas **21**, 056303 (2014).

[9]T. J. Awe, K. J. Peterson, E. P. Yu, R. D. McBride, D. B. Sinars, M. R. Gomez, C. A. Jennings, M. R. Martin, S. E. Rosenthal, D. G. Schroen, A. B. Sefkow, S. A. Slutz, K. Tomlinson, and R. A. Vesey, Phys. Rev. Lett. **116**, 065001 (2016).

[10]D. Colombant, W. Manheimer, and E. Ott, Phys. Rev. Lett. **53**, 446 (1984).

[11]R. E. Reinovsky, W. E. Anderson, W. L. Atchison, C. E. Ekdahl, R. J. Faehl, I. R. Lindemuth, D. V. Morgan, M. Murillo, J. L. Stokes, and J. S. Shlachter, IEEE Trans. Plasma Sci. **30**, 1764 (2002).

[12]A. R. Miles, Phys. Plasmas **16**, 032702 (2009).

[13]D. B. Sinars, S. A. Slutz, M. C. Herrmann, R. D. McBride, M. E. Cuneo, K. J. Peterson, R. A. Vesey, C. Nakhleh, B. E. Blue, K. Killebrew, D. Schroen, K. Tomlinson, A. D. Edens, M. R. Lopez, I. C. Smith, J. Shores, V. Bigman, G. R. Bennett, B. W. Atherton, M. Savage, W. A. Stygar, G. T. Leifeste, and J. L. Porter, Phys. Rev. Lett. **105**, 185001 (2010).

[14]D. B. Sinars, S. A. Slutz, M. C. Herrmann, R. D. McBride, M. E. Cuneo, C. A. Jennings, J. P. Chittenden, A. L. Velikovich, K. J. Peterson, R. A. Vesey, C. Nakhleh, E. M. Waisman, B. E. Blue, K. Killebrew, D. Schroen, K. Tomlinson, A. D. Edens, M. R. Lopez, I. C. Smith, J. Shores, V. Bigman, G. R. Bennett, B. W. Atherton, M. Savage, W. A. Stygar, G. T. Leifeste, and J. L. Porter, Phys. Plasmas **18**, 056301 (2011).

[15]Y. Y. Lau, J. C. Zier, I. M. Rittersdorf, M. R. Weis, and R. M. Gilgenbach, Phys. Rev. E **83**, 066405 (2011).

[16]M. E. Cuneo, M. C. Herrmann, D. B. Sinars, S. A. Slutz, W. A. Stygar, R. A. Vesey, A. B. Sefkow, G. A. Rochau, G. A. Chandler, J. E. Bailey, J. L. Porter, R. D. McBride, D. C. Rovang, M. G. Mazarakis, E. P. Yu, D. C. Lamppa, K. J. Peterson, C. Nakhleh, S. B. Hansen, A. J. Lopez, M. E. Savage, C. A. Jennings, M. R. Martin, R. W. Lemke, B. W. Atherton, I. C. Smith, P. K. Rambo, M. Jones, M. R. Lopez, P. J. Christenson, M. A. Sweeney, B. Jones, L. A. McPherson, E. Harding, M. R. Gomez, P. F. Knapp, T. J. Awe, R. J. Leeper, C. L. Ruiz, G. W. Cooper, K. D. Hahn, J. McKenney, A. C. Owen, G. R. McKee, G. T. Leifeste, D. J. Ampleford, E. M. Waisman, A. Harvey-Thompson, R. J. Kaye, M. H. Hess, S. E. Rosenthal, and M. K. Matzen, IEEE Trans. Plasma Sci. **40**, 3222 (2012).

[17]P. Zhang, Y. Y. Lau, I. M. Rittersdorf, M. R. Weis, R. M. Gilgenbach, D. Chalenski, and S. A. Slutz, Phys. Plasmas **19**, 022703 (2012).

[18]D. A. Yager-Elorriaga, P. Zhang, A. M. Steiner, N. M. Jordan, Y. Y. Lau, and R. M. Gilgenbach, Phys. Plasmas **23**, 101205 (2016).

[19]D. A. Yager-Elorriaga, P. Zhang, A. M. Steiner, N. M. Jordan, P. C. Campbell, Y. Y. Lau, and R. M. Gilgenbach, Phys. Plasmas **23**, 124502 (2016).

[20]D. A. Yager-Elorriaga, Y. Y. Lau, P. Zhang, P. C. Campbell, A. M. Steiner, N. M. Jordan, R. D. McBride, and R. M. Gilgenbach, Phys. Plasmas **25**, 056307 (2018).

[21]S. A. Slutz and R. A. Vesey, Phys. Rev. Lett. **108**, 025003 (2012).

[22]M. R. Weis, P. Zhang, Y. Y. Lau, P. F. Schmit, K. J. Peterson, M. Hess, and R. M. Gilgenbach, Phys. Plasmas **22**, 032706 (2015).

[23] T. J. Awe, R. D. McBride, C. A. Jennings, D. C. Lamppa, M. R. Martin, D. C. Rovang, S. A. Slutz, M. E. Cuneo, A. C. Owen, D. B. Sinars, K. Tomlinson, M. R. Gomez, S. B. Hansen, M. C. Herrmann, J. L. McKenney, C. Nakhleh, G. K. Robertson, G. A. Rochau, M. E. Savage, D. G. Schroen, and W. A. Stygar, Phys. Rev. Lett. **111**, 235005 (2013).

[24] R. D. McBride, M. R. Martin, R. W. Lemke, J. B. Greenly, C. A. Jennings, D. C. Rovang, D. B. Sinars, M. E. Cuneo, M. C. Herrmann, S. A. Slutz, C. W. Nakhleh, D. D. Ryutov, J.-P. Davis, D. G. Flicker, B. E. Blue, K. Tomlinson, D. Schroen, R. M. Stamm, G. E. Smith, J. K. Moore, T. J. Rogers, G. K. Robertson, R. J. Kamm, I. C. Smith, M. Savage, W. A. Stygar, G. A. Rochau, M. Jones, M. R. Lopez, J. L. Porter, and M. K. Matzen, Phys. Plasmas **20**, 056309 (2013).

[25] C. E. Seyler, M. R. Martin, and N. D. Hamlin, Phys. Plasmas **25**, 062711 (2018).

[26] C. E. Seyler and M. R. Martin, Phys. Plasmas **18**, 012703 (2011).

[27] D. A. Yager-Elorriaga, A. M. Steiner, S. G. Patel, N. M. Jordan, Y. Y. Lau, and R. M. Gilgenbach, Rev. Sci. Instrum. **86**, 113506 (2015).

[28] A. M. Steiner, P. C. Campbell, D. A. Yager-Elorriaga, K. R. Cochrane, T. R. Mattsson, N. M. Jordan, R. D. McBride, Y. Y. Lau, and R. M. Gilgenbach, Phys. Plasmas **25**, 032701 (2018).

[29] P. C. Campbell, T. M. Jones, J. M. Woolstrum, N. M. Jordan, P. F. Schmit, J. B. Greenley, W. M. Potter, E. S. Lavine, B. R. Kusse, D. A. Hammer, and R. D. Mcbride, Phys. Rev. Lett. **125**, 035001 (2020).

[30] L. Atoyan, D. A. Hammer, B. R. Kusse, T. Byvank, A. D. Cahill, J. B. Greenly, S. A. Pikuz, and T. A. Shelkovenko, Phys. Plasmas **23**, 022708 (2016).

[31] M. R. Weis, P. Zhang, Y. Y. Lau, I. M. Rittersdorf, J. C. Zier, R. M. Gilgenbach, M. H. Hess, and K. J. Peterson, Phys. Plasmas **21**, 122708 (2014).

[32] P. C. Campbell, J. M. Woolstrum, F. Antoulinakis, T. M. Jones, D. A. Yager-Elorriaga, S. M. Miller, N. M. Jordan, Y. Y. Lau, R. M. Gilgenbach, and R. D. Mcbride, IEEE Trans. Plasma Sci. **46**, 3973 (2018).

[33] R. D. McBride, C. E. Seyler, S. A. Pikuz, D. A. Hammer, D. J. Ampleford, T. A. Shelkovenko, and M. R. Martin, IEEE Trans. Plasma Sci. **39**, 2430 (2011).

[34] S. Lebedev, D. Ampleford, S. Bland, S. Bott, J. Chittenden, C. Jennings, M. Haines, J. B. Palmer, and J. Rapley, Nucl. Fusion **44**, S215 (2004).

[35] T. J. Smith, P. C. Campbel, N. M. Jordan, R. D. McBride, M. R. Gomez, M. D. Johnston, and G. R. Laity, Bull. Am. Phys. Soc. **64**, 317 (2019), http://flux.ap-s.org/meetings/YR19/DPP19/all_DPP19.pdf.

[36] E. Liverts and M. Mond, Phys. Plasmas **11**, 55 (2004).

[37] Z. Kolberg, E. Liverts, and M. Mond, Phys. Plasmas **12**, 062113 (2005).

[38] A. L. Velikovich, Phys. Fluids **3**, 492 (1991).

[39] R. D. McBride, T. A. Shelkovenko, S. A. Pikuz, D. A. Hammer, J. B. Greenly, B. R. Kusse, J. D. Douglass, P. F. Knapp, K. S. Bell, I. C. Blesener, and D. A. Chalenski, Phys. Plasmas **16**, 012706 (2009).

[40] G. C. Burdiak, S. V. Lebedev, R. P. Drake, A. J. Harvey-Thompson, G. F. Swadling, F. Suzuki-Vidal, J. Skidmore, L. Suttle, E. Khoory, L. Pickworth, P. de Grouchy, G. N. Hall, S. N. Bland, M. Weinwurm, and J. P. Chittenden, High Energy Density Phys. **9**, 52 (2013).